ACS Catalysis
Research Article
pubs.acs.org/acscatalysis

Mechanistic Insights into the Reduction of CO_2 on Tin Electrodes using in Situ ATR-IR Spectroscopy

Maor F. Baruch,[†] James E. Pander III,[†] James L. White, and Andrew B. Bocarsly*

Department of Chemistry, Princeton University, Princeton, New Jersey 08544, United States

ABSTRACT: The reduction of CO_2 on tin cathodes was studied using in situ attenuated total reflectance infrared spectroscopy (ATR-IR). Thin films of a mixed Sn/SnO_x species were deposited onto a single-crystal ZnSe ATR crystal. Peaks centered at about 1500, 1385, and 1100 cm^{-1}, attributed to a surface-bound monodentate tin carbonate species, were consistently present under conditions at which CO_2 reduction takes place. It was shown that these peaks are only present at potentials where CO_2 reduction is observed. Moreover, these peaks disappear if the pH of the reaction is too low or if the tin surface is chemically etched to remove surface oxide. $Sn_6O_4(OH)_4$ and SnO_2 nanoparticles were shown to be catalytically active for CO_2 reduction, and insights into the oxidation state of the catalytically active species are gained from a comparison of the catalytic behavior of the two nanoparticle species. From these experiments, a mechanism governing the reduction of CO_2 on tin electrodes is proposed.

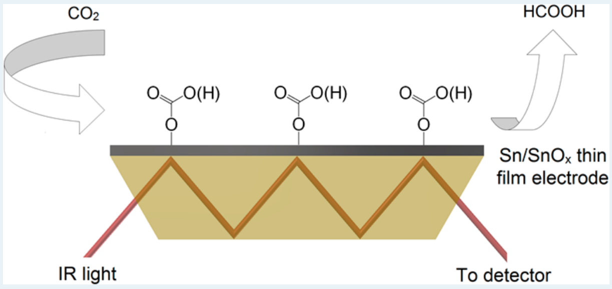

KEYWORDS: *carbon dioxide reduction, IR spectroelectrochemistry, tin oxides, tin electrochemistry, tin oxide nanoparticles*

1. INTRODUCTION

Atmospheric concentrations of CO_2 have increased from 280 ppm to over 400 ppm since 1850.[1] The Intergovernmental Panel on Climate Change (IPCC) claims that this increase is largely due to the anthropogenic use of fossil fuels such as coal, oil, and natural gas.[2] Potential consequences of the heightened greenhouse concentrations include changes in average surface temperature, global mean sea level rise, ocean acidification, and perturbations to natural ecosystems.

The electrochemical reduction of CO_2 to value-added products has been widely studied as a possible technique for the mitigation of atmospheric CO_2. However, CO_2 is an extremely stable species, and its activation and reduction are far from trivial.[3] Nonetheless, reports on the reduction of CO_2 using metallic, semiconducting, and molecular catalysts have been widely published in the literature.

Numerous reports dealing with the CO_2 reduction chemistry of Sn electrodes have been published recently. Reports on the way in which pH affects the measured product distribution[4] and on the surface degradation and deactivation of various tin catalysts[5] have recently surfaced. Chen and Kanan showed that etching off the native oxide layer from tin electrodes decreased their ability to act as CO_2 reduction catalysts and that electrodeposited Sn/SnO_x layers are more catalytic than bulk tin electrodes.[6] At low overpotential, it was asserted that the mechanism proceeds via a reversible electrochemical step in which CO_2 is reduced to $CO_2^{\bullet-}$ followed by a rate-limiting chemical step.[6] A similar oxide dependence has been shown to be prevalent on gold and indium electrodes.[7,8] Despite these works, the key surface species associated with CO_2 reduction at tin have not been identified, and it is unknown whether morphological or oxide-specific factors contribute to the enhanced catalytic behavior.

Herein, we present in situ spectroscopic evidence which suggests that surface oxides of Sn are present in the course of CO_2 reduction and are a key factor in the observed catalytic formation of formate. Additionally, we report the direct observation of a surface carbonate species that is present at Sn interfaces specifically when carbon dioxide reduction takes place. The potential and pH dependence of this species are evaluated. Insights into the oxidation state of the active Sn center are assessed with the use of various tin oxide nanoparticle catalysts that were drop-cast onto glassy carbon electrodes. On the basis of these observations, the roles of both the surface oxide and carbonate are elucidated.

2. EXPERIMENTAL METHODS

2.1. Deposition of Sn Thin Films onto the ZnSe ATR-IR Crystal. Sn was deposited onto a ZnSe ATR-IR crystal (Pike Technologies) using a VCR IBS/TM250S ion beam sputterer. Ar^+ was used as the sputtering gas. A strip of Sn foil (Sigma-Aldrich, 99.998%) was used as a sputter target. The mass of the deposited layer was measured using a quartz crystal microbalance. In all experiments, a 200 nm film was deposited at an approximate rate of 0.2 Å s^{-1}. The crystal was prepared using 1 μm (Aldrich, 99.5%) and <50 nm (Aldrich) grades of alumina to clean the surface. Mechanical polishing using diamond paste (1, 0.50, and 0.25 μm, Glennel, Electron Microscopy Sciences)

Received: February 24, 2015
Revised: April 13, 2015
Published: April 13, 2015

DOI: 10.1021/acscatal.5b00402
ACS Catal. 2015, 5, 3148−3156

was used to restore the ATR crystal's optical quality. In experiments requiring a Sn^0 surface, HBr (33% in acetic acid, Sigma-Aldrich) diluted 3× was used to etch the native SnO_x off the deposited Sn layers.[9] *Caution*! Toxic H_2Se gas may be evolved if the acid comes in contact with the underlying ZnSe.[10]

2.2. In Situ ATR-IR Spectroscopy. A custom-made electrochemical cell which fit on top of the ATR crystal was machined out of polytetrafluoroethylene (PTFE). The thin films of deposited Sn acted as the working electrodes. Electrical contact to the thin layers was made using conductive copper tape placed on the outer edge of the ZnSe crystal. In all experiments, 0.1 M K_2SO_4 was used as a supporting electrolyte. The potential applied to the working electrode was controlled via a CH Instruments 760D potentiostat/galvanostat. Pt gauze (Sigma, 99.9%) was used as an auxiliary electrode. All potentials are referenced to the Ag/AgCl (3 M NaCl) half-cell. The resistance across the deposited tin layer was tested with an ohmmeter before and after each experiment in order to verify that the cathode did not degrade during the course of the experiment. In each case, the measured resistance was $<0.1\ \Omega$.

ATR-IR spectra were collected with a Nicolet 6700 FTIR using a liquid nitrogen cooled MCT detector. The spectrometer was fitted with a single-bounce VeeMAX II ATR apparatus (Pike Technologies) set at a 60° reflection angle. Data were collected using the Omnic software package. In a typical in situ ATR-IR experiment, Ar gas (AirGas) was bubbled through an aqueous solution containing 0.1 M K_2SO_4 for at least 30 min. The solution was transferred to the electrochemical cell fitted with the working, counter, and reference electrodes. Ar was constantly bubbled into solution in order to prevent atmospheric CO_2 or O_2 from entering the cell. A potential was applied to the working electrode, and IR spectra were collected until a time-independent signal was obtained (typically 20−30 min). A background spectrum was collected at this point, and a constant purge of CO_2 was bubbled into the cell. Time-dependent spectra were collected until the system reached equilibrium with respect to any adsorbed species. Typically, 16 scans were collected for each spectrum at a resolution of 1 cm^{-1}.

2.3. Surface Characterization of the ATR-IR Crystal. A polished 13 mm diameter × 1 mm thick ZnSe optical disk (Alfa Aesar) was used as a test substrate for surface characterization and analysis. X-ray photoelectron spectroscopy (XPS) was carried out using a VG Scientific MK II ESCALab utilizing a magnesium X-ray source. A hemispherical analyzer with a 20 eV pass energy was used as the detector. Analysis of the resulting spectra was conducted via the CasaXPS software package. Peaks were fit to hybrid Gaussian/Lorentzian curves. Scanning electron microscopy (SEM) images and energy dispersive X-ray (EDX) spectra were obtained using a Quanta 200 FEG ESEM or an XL-30 FEG-SEM.

2.4. Electrochemistry of Bulk Tin Electrodes. Tin disk electrodes used for cyclic voltammetric analysis were fabricated by encapsulating a 2 mm diameter tin wire (Alfa Aesar, 99.9985%) in a hollow polytetrafluoroethylene tube (McMaster Carr). These disks were polished before use with a slurry of 1 μm alumina (Electron Microscopy Sciences). Electrolysis experiments using electrodes formed from tin foils were conducted in a custom-made Pyrex four-neck round-bottom flask with a total volume of 60 mL. In each experiment, approximately 30 mL of electrolyte solution was used. Tin foil (Sigma, 99.9%) was cut into 1 cm × 1 cm squares, and these foils (A = ca. 2 cm^2) were used as working electrodes. A platinum mesh housed in a gas dispersion tube (Ace Glass, 4−8 μm porosity) was used as an auxiliary electrode. An aqueous Ag/AgCl electrode (3 M NaCl) was used as a reference, and all potentials are quoted with respect to this reference half-cell throughout. All three electrodes were placed into the electrochemical cell via gastight Chem-Thread #7 joints supported by Viton O-rings. Electrodes were prereduced at the electrolysis potential in an Ar-purged electrolyte solution for 20 min in order to more closely mimic the ATR-IR conditions. Faradaic efficiencies for hydrogen and CO formation were based on gaseous aliquots which were removed from the electrolysis cells through a GL-14 cap fitted with a gastight silicone septum (Ace Glass) using a 25 μL GC syringe (Hamilton). Each electrolysis experiment was run so that at least 4 C of charge passed through the working electrode, and each trial was repeated in triplicate. Faradaic efficiencies are plotted as the average of these three runs ± one standard deviation.

2.5. Synthesis, Characterization, and Preparation of Tin Oxide Nanoparticle Electrodes. $Sn_6O_4(OH)_4$ and SnO_2 nanoparticles were synthesized by dissolving the respective chloride salts ($SnCl_2$, Alfa Aesar, 99%; $SnCl_4\cdot 5H_2O$, J.T. Baker, 99%) in water at a concentration of 0.4 M, adding 0.4 M NH_4OH (J. T. Baker, 29%) dropwise until a precipitate formed, and then adding 2 M NH_4OH dropwise until the pH exceeded 9. This method was adapted from that of Chandradass for the synthesis of indium oxide nanoparticles.[11] The pale red Sn^{II} precipitate and the white Sn^{IV} precipitate were each centrifuged and rinsed several times under N_2 with 2-propanol (Sigma-Aldrich, 99.9%), followed by drying under vacuum at room temperature to limit exposure to air and preserve the tin oxidation state. A portion of the Sn^{IV} precipitate was calcined at 600 °C for 4 h in air and yielded a yellow powder. X-ray powder diffraction (XRD) was performed on each of the three sets of particles using a Rigaku Miniflex II X-ray diffractometer with Cu Kα radiation to confirm their identities. Transmission electron microscopy (TEM) images of each powder were obtained with a Philips CM100 TEM at an accelerating voltage of 100 kV.

The nanoparticles were supported on Vulcan XC-72 carbon black at ∼35 wt % Sn by sonication in 2-propanol for 1 h. A small amount of LIQUion solution (Ion Power, Inc., 15 wt %) was added to the catalyst ink to maintain catalyst layer stability on the electrode surface. For each experiment, 10 μL of the catalyst colloid (∼0.1 mg total) was drop-cast onto a polished glassy carbon disk (0.3 cm diameter, Bioanalytical Systems, Inc.), with the liquid allowed to evaporate between each drop.

2.6. Product Detection and Quantitation. Gaseous products were analyzed with either an HP 5890 or an HP 6890 gas chromatograph (molecular sieve column CP7538) connected to an eDAQ PowerChrom 280 system and software package. The column head pressure was held at 32 psi. The oven, injector, and detector temperatures were held at 70, 250, and 300 °C, respectively. The instrument was calibrated for both CO and H_2 using no fewer than 30 standards prepared from a CO/H_2 mixture (AirGas). The response was found to be linear in the region of interest. Liquid products were identified and quantitated with an internal standard in a Bruker 500 MHz ^1H NMR instrument with a cryoprobe detector and a custom solvent suppression pulse sequence.

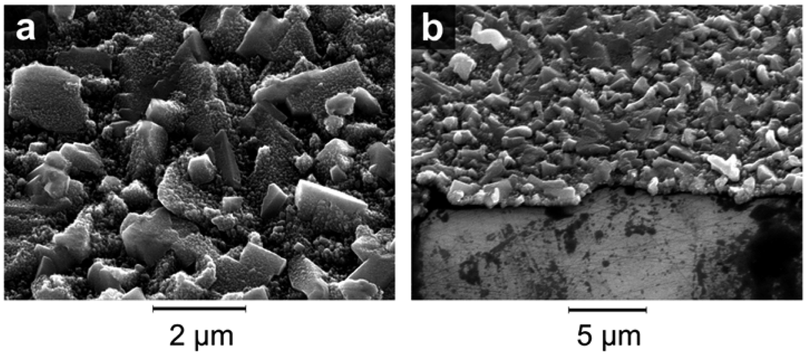

Figure 1. SEM images (45° viewing angle) of (a) a 200 nm Sn layer deposited onto a ZnSe single crystal substrate and (b) the interface between the deposited Sn layer (top) and the underlying ZnSe substrate (bottom).

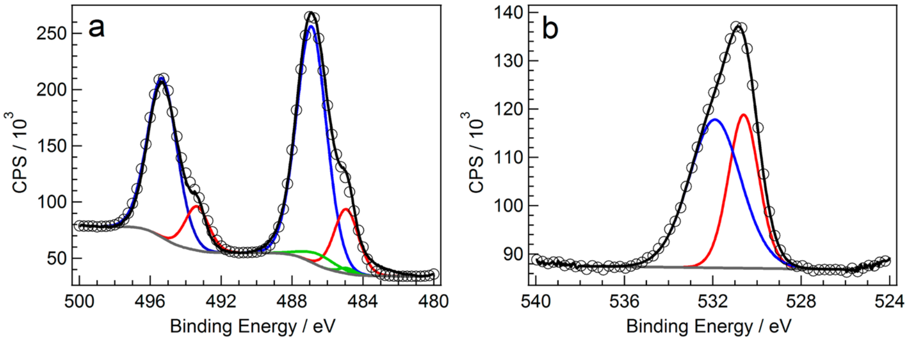

Figure 2. XPS of the ATR-IR crystal on which a 200 nm thin film of Sn was deposited. In both spectra, the open circles represent the raw data and the black solid lines provide the numerical fit. (a) Sn 3d region. The two blue peaks represent the $3d_{3/2}$ (left peak) and $3d_{5/2}$ (right peak) features of an oxidized $Sn^{II/IV}$ species. The red peaks represent the $3d_{1/2}$ (left) and $3d_{5/2}$ (right) features of a metallic Sn state. The two green peaks are satellites of the two $3d_{1/2}$ peaks that arise due to the nonmonochromaticity of the X-ray source used to obtain the spectra ($\Delta = 8.40$ eV). (b) O 1s region. The red and blue curves correspond to Sn^{II}/Sn^{IV} oxides and a $Sn(OH)_x$ species, respectively.

3. RESULTS AND DISCUSSION

3.1. Surface Characterization of the ZnSe/Sn Surface.

Figure 1 shows SEM images at 45° of a 200 nm Sn layer deposited onto a ZnSe single-crystal substrate. The layer was found to be rough with surface features on the order of 1−2 μm. Closer inspection of the SEM in Figure 1a reveals that the surface is additionally covered in Sn nanoparticles on the order of 50−200 nm. Figure 1b shows a cross section of the Sn/ZnSe interface. The underlying ZnSe surface is smooth and can be seen in the bottom of the micrograph. The rough Sn surface can be seen toward the top of the micrograph. EDX analysis shows the presence of C (27.86%), Zn (37.47%), and Se (34.68%) on the ZnSe crystal. No other elements were found to be present. The ratio of Zn to Se is close to the expected value on the basis of the stoichiometry of the crystal. The high carbon content of this particular ZnSe sample is likely due to residual carbon from the carbon tape that was used to block the lower part of the crystal during the deposition process. An EDX analysis of the deposited Sn layer shows that the surface contains Sn (53.70%), O (34.14%), and C (12.16%). No other elements, including Zn and Se, were present.

XPS of a 200 nm tin layer deposited on a ZnSe single crystal is shown in Figure 2. The Sn 3d region is highlighted in Figure 2a. Deconvolution suggests that two Sn species are present on the deposited surface. A doublet at 495.3 and 486.9 eV is assigned to the $3d_{3/2}$ and $3d_{5/2}$ peaks of tin in a mixed tin oxide. This assignment is consistent with that made by Chao et al., who assigned peaks at 487.16 and 486.80 eV to the Sn $3d_{5/2}$ transitions in SnO_2 and SnO, respectively.[12] Due to the resolution of the spectrometer employed, the tin transitions for these two oxides could not be differentiated.

Two more peaks appear at binding energies of 493.4 and 484.9 eV and are assigned to the $3d_{3/2}$ and $3d_{5/2}$ peaks of Sn^0. These values are in agreement with the assignment made by Chao.[12] For both species, a spin−orbit splitting of 8.42 eV is observed between the $3d_{3/2}$ and $3d_{5/2}$ peaks, as has been reported in the literature.[13] Integration of the spectral signal indicates that 81.9% of the tin atoms present on the surface of the ZnSe/Sn electrode are oxidized, while the remaining 18.1% are in the Sn^0 oxidation state, in agreement with Kanan's report for similar CO_2 reduction catalysts.[6] The final set of peaks, observed at 486.9 and 485.0 eV, is artifactual and corresponds to the overtone peaks originating from the Sn $3d_{3/2}$ peaks due to the nonmonochromaticity of the Mg X-ray source.

The O 1s region of the XPS spectrum is depicted in Figure 2b. The spectrum was fit to two oxygen-containing species with transitions centered at 530.6 and 531.9 eV. The first peak is consistent with the presence of Sn^{II}/Sn^{IV} oxides, as reported by Tselesh.[14] The second peak is assigned to a Sn−OH species (531.1 ± 0.6 eV), which is consistent with the XPS reported for indium CO_2 reduction catalysts.[8,14]

Detailed XPS scans in the regions where the Zn 2p and Se 3d peaks would appear (1020−1050 and 50−65 eV, respectively) were flat and devoid of any features.[15] This finding, in conjunction with the EDX analysis, demonstrates that the ZnSe ATR-IR crystal is completely covered with Sn^0/SnO_x and that neither Zn nor Se is present on the catalytic surface. For this reason, we can ascribe the spectral data (see sections 3.2 and

3.3) to the chemistry occurring strictly at the Sn/SnO_x layer and not to interference due to the presence of either Zn or Se.

3.2. In Situ ATR-IR Spectroscopy on Sn in the Presence of Ar. In order to probe the electrochemistry of the oxide layer, ATR-IR spectra were collected under an argon atmosphere at two different potentials (Figure 3). At an applied potential of −1.4 V (Figure 3a), peaks in the IR spectra at 3500 and 1650 cm^{-1}, which are assigned to water vibrations, are observed to grow in slowly with time. This phenomenon has previously been attributed to the slow reduction of the native oxide layer, which exposes more water to the sampling region of the evanescent wave of the IR beam.[8] As the oxide layer thickness approaches a steady state, as evidenced by the slow rate of change in the spectra at −1.4 V, a background is taken and the potential is stepped to −1.6 V (Figure 3b). Again, the same peaks slowly emerge, indicating that, while the layer would not continue to reduce at an appreciable rate at −1.4 V, there is still an oxide layer present, and further reduction of the oxide layer takes place at this more negative potential. The tin Pourbaix diagram indicates that tin oxides are thermodynamically unstable at these potentials.[16] However, the Pourbaix diagram depicts only the thermodynamically most stable phase at a given pH and potential without consideration of the kinetics and the dynamic nature of the system. The data presented in Figures 3 and 5 clearly indicate the presence of a metastable oxide at −1.4 V, as has been similarly observed previously for the In/In$(OH)_3$/In_2O_3 interface.[8] If one wishes to understand the electroactive nature of the tin interface, then these metastable oxides must be taken into account.

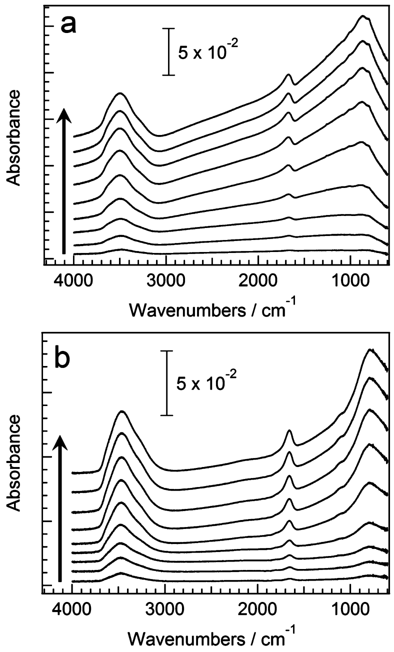

Figure 3. Time-dependent ATR-IR spectra in the presence of Ar taken at 1, 3, 5, 10, 20, 30, 40, 50, and 60 min: (a) −1.4 V vs Ag/AgCl with a background taken at the same potential at t = 0 min; (b) −1.6 V vs Ag/AgCl with a background taken after 60 min of reduction at −1.4 V. In both parts of the figure, the arrow shows the direction of spectral evolution with time.

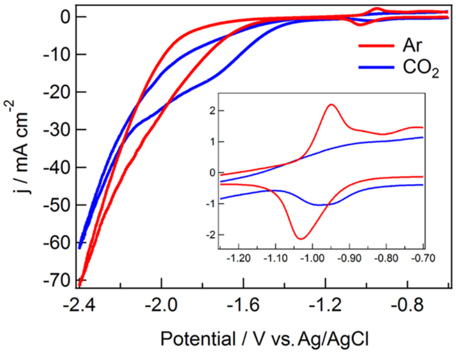

Figure 4. Cyclic voltammograms on tin disks in the presence of Ar (red) and CO_2 (blue). The pH of the electrolyte was 4.4, and the potential was scanned at a rate of 100 mV s^{-1}. In the Ar scan, a redox feature appears at $E_{1/2}$ = −1.0 V vs Ag/AgCl (inset). This feature is diminished and is no longer reversible under CO_2.

Figure 4 shows a cyclic voltammogram of a polished tin disk electrode in Ar (red) and CO_2 (blue) saturated aqueous solutions at pH 4.4 at a scan rate of 100 mV s^{-1}. The most immediately obvious feature is a shoulder starting around −1.4 V in a CO_2 saturated solution which is absent under argon. This type of current response is commonly associated with the reduction of CO_2 to reduced products: in this case CO and formic acid.[3] The second feature of interest is a set of waves with $E_{1/2}$ at −1.0 V and a peak-to-peak separation of 100 mV. Similar redox features have been observed at −0.75 V in pH 7.5 borate buffer solutions and have been attributed to the reduction of SnO_2 to a mixed Sn^{II} oxide/hydroxide and its subsequent reoxidation.[17] When adjusted for pH, the redox couple would be anticipated to appear at the observed redox potential shown in Figure 4. Interestingly, when the voltammetry is performed in a CO_2 saturated solution at 100 mV s^{-1}, the reduction wave diminishes in magnitude while the reoxidation wave disappears completely. At faster scan rates, the reoxidation wave reappears, indicating that there is a competing chemical process occurring in the presence of CO_2 that prevents the reoxidation of the Sn^{II} species. Similar behavior has been previously reported on indium cathodes, where a redox feature in this region was identified as an In_2O_3/In^0 couple.[8] Cyclic voltammetry utilizing the tin cathode employed for ATR experiments was conducted in Ar- and CO_2-purged solutions and yielded comparable features.

In order to test the reversibility of the thinning of the native oxide layer, an experiment was performed where the potential was stepped across this redox couple in order to observe the changes in water signal. The potential was stepped to −1.2 V, which is more negative than the redox feature shown in Figure 4. The potential was then held at −1.2 V, where a background was taken before the potential was stepped to −1.6 V (Figure 5a). Here, a large increase in the water signals at 3500 and 1650 cm^{-1} indicates that there is a significant thinning of the oxide layer. When the potential was then jumped to −0.8 V, which is more positive than the redox couple observed in the cyclic voltammogram, the vibrational modes associated with the water were observed to decrease and take on negative values in the difference spectrum (Figure 5b). This is interpreted as a thickening of the oxide layer, which excludes water that had previously been in the ATR-IR sampling region. Thus, the thinning of this oxide layer is reversible, and it is possible to qualitatively control the thickness of the native oxide layer simply by applying the appropriate external bias. The native oxide layer on tin has been previously implicated as playing an important role in the mechanism of CO_2 reduction on tin cathodes.[6]

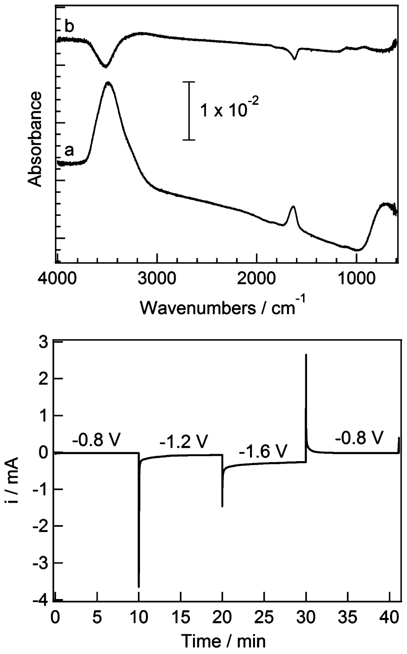

Figure 5. (Top) ATR-IR spectra demonstrating the reversible thinning of the SnO_x layer: (a) scan taken at −1.6 V with a background at −1.2 V; (b) scan taken at −0.8 V with a background at −1.6 V. (bottom) Annotated current−time trace of the potential jumps described above.

3.3. In Situ ATR-IR Spectroscopy on Sn in the Presence of CO_2.

When CO_2 is introduced to the cell at −1.4 V, new absorption features become evident in the ATR-IR spectrum. A doublet of peaks centered at 2350 cm^{-1}, corresponding to gaseous CO_2, immediately becomes evident, as has been reported in previous in situ ATR-IR studies.[8] Additionally, intense peaks at 1500 and 1385 cm^{-1}, as well as a weak peak at 1100 cm^{-1}, are observed in addition to the water peaks previously discussed, as shown in Figure 6. As the potential is gradually stepped down from −1.0 to −1.4 V in order to prevent delamination of the tin layer from the ATR crystal, the current becomes more negative in a stepwise fashion. The large transient current spikes are due to double-layer charging effects (Figure 6b). However, a large increase in the cathodic current is observed as CO_2 is introduced into the cell, indicating that a new Faradaic process is taking place. Table 1 summarizes the vibrational stretches of a variety of relevant species. Of particular note, free carbonate ions typically show a single strong absorption between 1470 and 1420 cm^{-1}. Monodentate tin carbonate species have been reported to show two strong absorptions at 1530−1470 and 1370−1300 cm^{-1}, while bidentate tin carbonates show a strong absorption at a higher wavenumber.[18,19] Similarly, dimethyltin carbonate polymers have been reported to have strong absorptions associated with tin carbonate at 1510, 1385, and 1105 cm^{-1}.[20,21] On the basis of these literature reports, we conclude that the observed stretches do not correspond to carbonate ions in solution, as have been reported in other in situ studies,[22,23] and instead correspond to a surface-bound tin carbonates.

Table 1. Summary of IR Stretches (cm^{-1}) for Various Carbonate, Formate, and Carboxylate Species

species	1650−1550 cm^{-1}	1550−1450 cm^{-1}	1450−1350 cm^{-1}	1350−1250 cm^{-1}	1250−1150 cm^{-1}	1150−1050 cm^{-1}
present study		1500	1385	1265		1100
CO_3^{2-} (aq)[18]			1450			
HCO_3^- (aq)[18]	1640			1300	1220	
RCO_2^- (aq)[18]	1580		1360			
Sn-CO_3^- (monodentate)[18]		1500	1370			
Sn-CO_3^- (bidentate)[18]	1610			1265		
dimethyl Sn carbonate polymers[20,21]		1510	1385			1105
$Sn(OOCH)_2$[18]	1563		1385	1339		
HCOOH (aq)[18]	1575			1350	1250	

Although these data unambiguously indicate the presence of a surface-bound carbonate species under conditions relevant to CO_2 reduction, it is not immediately apparent if this species is a reducible intermediate or if the formation of this carbonate is a necessary surface modification that is catalytic for CO_2 reduction.

In order to distinguish between these possibilities, a series of experiments were performed in which the electrochemical conditions were varied so that CO_2 reduction could be turned on or off. After observation of the tin carbonate peaks at −1.8 V, the CO_2 purge was replaced with an Ar purge, while the potential remained static. The results of this experiment are shown in Figure 7. It is observed that the tin carbonate peaks slowly decrease over the course of 1 h as CO_2 is slowly removed from the electrochemical cell. Simultaneously, it is

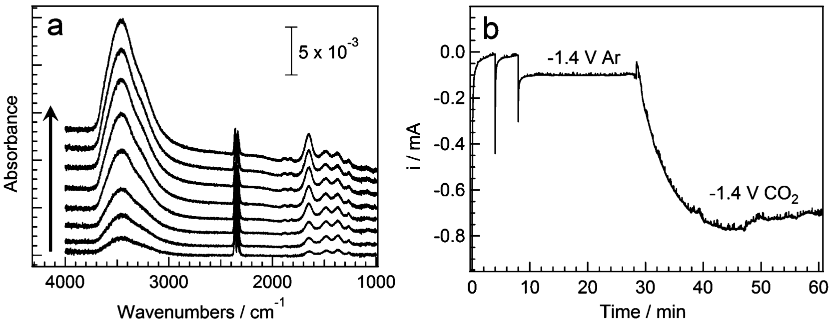

Figure 6. (a) In situ time-dependent ATR-IR spectra at −1.4 V vs Ag/AgCl. Time points were taken at 1, 3, 5, 10, 15, 20, 25, and 30 min after the introduction of CO_2 into the cell. The black arrow shows the direction of evolution with time. (b) Current−time trace obtained during the acquisition of the spectra in (a). The two current spikes correspond to the gradual decrease in potential (from −1.0 to −1.4 V in 0.2 V decrements). The large increase in cathodic current is due to the introduction of CO_2 into the cell at *t* = 30 min.

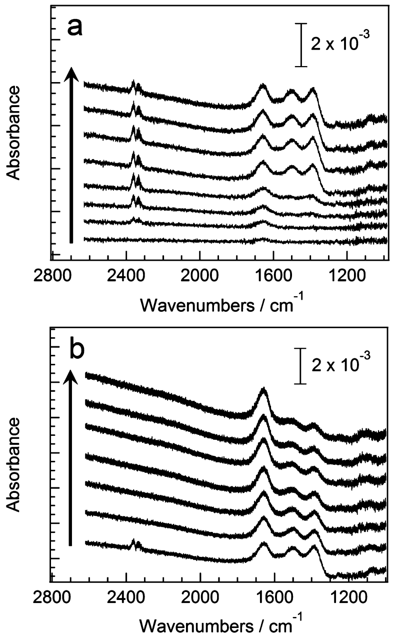

Figure 7. Time-dependent ATR-IR spectra at −1.8 V vs Ag/AgC: (a) emergence of carbonate signals upon the introduction of CO_2 to the electrochemical cell, with traces taken 0, 1, 3, 5, 15, 20, 25, and 30 min after the introduction of CO_2; (b) reduction of the carbonate signal upon removal of CO_2 from the electrochemical cell, with traces corresponding to time points 0, 10, 20, 30, 40, 50, and 60 min after the removal of CO_2 and introduction of Ar into the electrolyte. In both figures, the arrow shows the direction of evolution with time.

observed that the cathodic current decreases on the same time scale that the carbonate peaks diminish in intensity in the IR spectra. This experiment suggests that the direct reduction of the carbonate is more plausible, as the carbonate species would be expected to remain on the electrode surface if it were a catalytic modification for the reduction of aqueous CO_2.

Additionally, the potential was varied between values where CO_2 reduction is expected to occur and those where CO_2 reduction is not anticipated to occur, as confirmed by potentiostatic bulk electrolysis experiments performed on tin foil electrodes (Figure 8b). As shown in Figure 8a, both at open circuit and at −1.0 V, no carbonate species are observed; however, as the potential is stepped to −1.4 and −1.8 V, the carbonate species are evident before disappearing again at −2.4 V, where primarily hydrogen is evolved.

Figure 9 demonstrates the impact of eliminating the presence of the native oxide both via chemical etching with HBr and of lowering the experimental pH to one where only H_2 is electrochemically generated. If the surface oxide of the tin layer is removed using HBr, no peaks corresponding to carbonate formation are observed (Figure 9b). This corresponds to conditions where little to no CO_2 reduction is observed, as demonstrated by Chen and Kanan.[6] Additionally, the observed carbonate peaks disappear upon dropping the pH of the electrolyte from 4.4 to 1.5 by addition of H_2SO_4 (Figure 9c).

In summary, in situ ATR-IR spectroscopy of an electrochemical cell demonstrate that, under conditions at which CO_2 reduction occurs, strong vibrational stretches are observed that can be attributed to a surface-bound tin−carbonate species. After experiments under the same conditions at which the carbonate is found in situ, formate is detected ex situ via ^1H NMR, even though no formate stretches appear in the ATR-IR spectra. If the chemical or electrochemical conditions are altered in any way that prevents CO_2 reduction from occurring, these vibrational stretches are significantly reduced or disappear completely. Thus, we conclude that, taken together, these experiments suggest a surface-bound tin−carbonate species is an active intermediate in the electrochemical reduction of CO_2 at an aqueous tin interface.

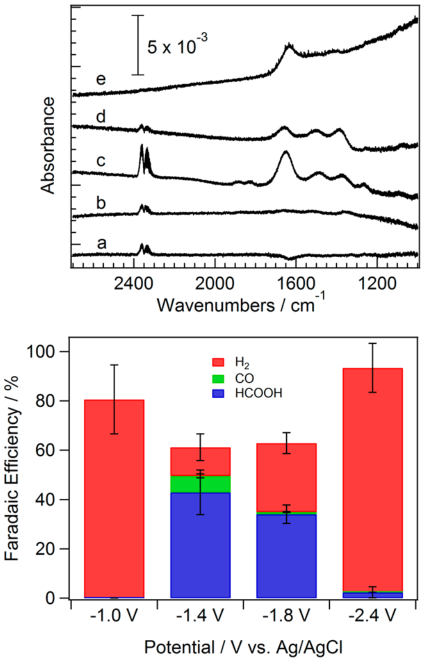

Figure 8. (top) In situ ATR-IR spectra taken in the presence of CO_2 at various electrochemical potentials: (a) open circuit; (b) −1.0 V; (c) −1.4 V; (d) −1.8 V; (e) −2.4 V. (bottom) Product distribution from the reduction of CO_2 on prereduced bulk electrodes. The red, green, and blue bars correspond to the Faradaic efficiencies of H_2, CO, and formate, respectively.

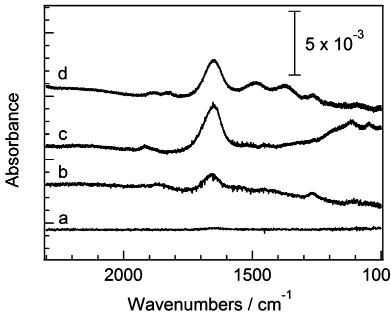

Figure 9. ATR-IR traces at −1.4 V vs Ag/AgCl under various chemical conditions and treatments: (a) background; (b) HBr-etched Sn surface; (c) pH 1.5; (d) normal operating conditions (nonetched surface, pH 4.4). All spectra were taken under CO_2 with Ar as a background.

3.4. Characterization, Voltammetry, and Electrolysis of Tin Oxide Nanoparticles. The tin oxide nanoparticles were characterized using both XRD and TEM (Figures 10 and 11, respectively). The pattern of the pale red Sn^{II} powder matched that of a hydrated tin(II) oxide[24] with the chemical formula $Sn_6O_4(OH)_4$. These nanoparticles were 10−60 nm in diameter and clumped together to form large aggregates on the TEM grid. The diffraction pattern of the yellow Sn^{IV} powder

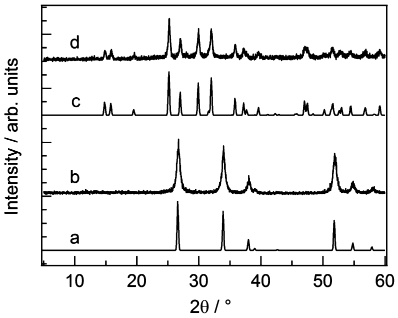

Figure 10. XRD patterns for the nanoparticle catalysts used in this study: (a) bulk SnO_2;[25] (b) SnO_2 nanoparticles; (c) bulk $Sn_6O_4(OH)_4$;[24] (d) $Sn_6O_4(OH)_4$ nanoparticles. Literature patterns are included for comparison.

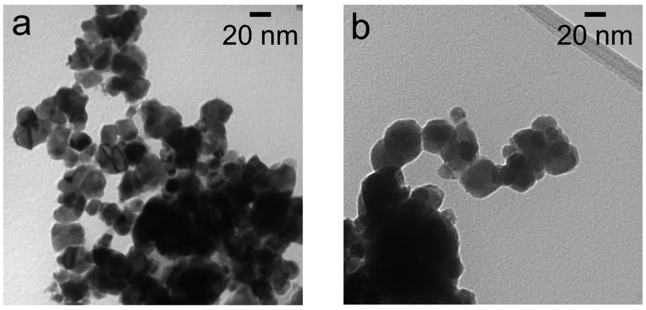

Figure 11. TEM images: (a) SnO_2 nanoparticles; (b) $Sn_6O_4(OH)_4$ nanoparticles.

matched the literature pattern of rutile SnO_2.[25] The SnO_2 nanoparticles were typically 10−30 nm in diameter.

Potentiostatic bulk electrolysis experiments were performed on glassy carbon electrodes modified with $Sn_6O_4(OH)_4$ and SnO_2 nanoparticle inks at a variety of potentials; the Faradaic efficiencies for each product are shown in Figure 12. It is observed that, at potentials less than or equal to −1.6 V, there is statistically no difference in the product distributions for $Sn_6O_4(OH)_4$ and SnO_2. However, at −1.4 V, it is observed that the SnO_2 nanoparticles produce significantly less formic acid than the $Sn_6O_4(OH)_4$ nanoparticles. This result may suggest that the active species for catalysis is a Sn^{II} species instead of a Sn^{IV} species. As previously noted for tin surfaces (section 3.2), at −1.4 V, the reduction of the oxide layer does not go to completion on the time scale of the experiment. At more negative potentials, it is anticipated that SnO_2 is reduced to a Sn^{II} oxyhydroxide to a greater extent, and this explains the similarity between the product distributions. Otherwise, the electrolysis results for the nanoparticles mirror those on polycrystalline tin foils and in the ATR-IR data shown in Figure 8.

3.5. Mechanism of CO_2 Reduction on Sn/SnO_x.

There has been significant interest in determining the mechanism of CO_2 reduction on a variety of metallic electrode materials.[3,26] In particular, the product distribution at a variety of pHs, potentials, electrolytes, CO_2 pressures, temperatures, and electrode preparation methods have been thoroughly investigated for tin cathodes.[4,6,27−29] However, despite previous work, details regarding a specific mechanism are minimal. It has historically been accepted that the electrochemical reduction of CO_2 on tin cathodes proceeds through an adsorption equilibrium step followed by a rate-determining one-electron reduction to the $CO_2^{\bullet-}$ species, which undergoes a proton-coupled electron transfer.[30] It is generally noted that, thermodynamically, the reduction of CO_2 to $CO_2^{\bullet-}$ occurs at −2.1 V vs Ag/AgCl.[31−33] However, tin is observed to reduce CO_2 at potentials significantly less negative.[4−6,34] This discrepancy is generally explained by assuming that the surface-dependent nature of this reaction shifts ΔG_{rxn} from the calculated value; However, there is little insight into what the reduction potential of this species is expected to be. The main support for the historical mechanism is the interpretation of Tafel slopes. Despite this, there have been significant and notable deviations in published Tafel slopes for tin systems which weaken the mechanistic conclusions that have been presented. Specifically, Kapusta and Hackerman reported a Tafel slope of 115 mV/decade for potentials more positive than −1.45 V vs SCE.[30] The interpretation of this Tafel slope suggests that the reaction occurs via a CE mechanism described previously, though Hackerman does not accurately account for the partial current densities of all reaction products. More recently, Chen and Kanan addressed these experimental issues and reported a Tafel slope of 74 mV/decade over a comparable potential window.[6] This Tafel slope is significantly smaller than the slope presented by Hackerman and has been interpreted to suggest an EC mechanism involving a reversible one-electron transfer to form $CO_2^{\bullet-}$ followed by a chemical rate-determining step, which is possibly a protonation.[6] It is important to note that a single Tafel slope could point toward a number of mechanisms, as outlined by Fletcher.[35] A slope of 74 mV/decade could also be ascribed to a CE mechanism in which the electrochemical step involves a two-electron transfer, which, given the high barrier to forming the one-electron-reduced $CO_2^{\bullet-}$ radical, is more likely than a reversible initial electrochemical step. Given the uncertainties in the Tafel data, along with the ambiguities in the mechanistic interpretation of Tafel slopes, it is challenging to use such an

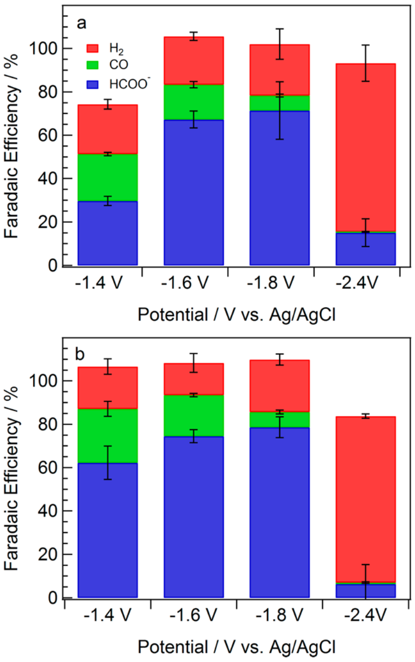

Figure 12. Potential-dependent product distributions for the reduction of CO_2 on glassy carbon electrodes modified with (a) SnO_2 nanoparticles (b) $Sn_6O_4(OH)_4$ nanoparticles. In both figures, the red, green, and blue bars correspond to the Faradaic efficiencies of H_2, CO, and formate, respectively.

approach in the determination of key intermediates in the reduction of CO_2.

The data presented in this work directly indicate that the surface-bound tin carbonate is relevant in the mechanism for CO_2 reduction at tin electrodes under native electrochemical conditions. Our group has recently demonstrated a similar behavior on indium cathodes,[8] and a similar intermediate has been proposed on metal-loaded Ga_2O_3.[36] Thus, we propose that the formation of a surface-bound tin carbonate is the key chemical step involved in the reduction of CO_2 on tin. As outlined in Scheme 1, we propose that the reduction of CO_2 is preceded by a two-electron reduction of the electrode from a native SnO_2 to a Sn^{II} oxyhydroxide, which is the catalytic resting state. The ATR-IR spectra at open circuit and −1.0 V in the presence of CO_2 show no carbonate peaks, indicating that the SnO_2 layer must first be reduced at potentials more negative than the voltammetrically observed half-wave potential, to a Sn^{II} species. This species can then react with CO_2 to form the observed surface-bound carbonate. The tin carbonate undergoes the necessary transfers of two electrons and a proton to form formate, which quickly desorbs to return the surface to the Sn^{II} oxyhydroxide surface, as evidenced by the lack of formate absorption bands in the IR spectra. This reaction scheme supports a CE mechanism, with a chemical equilibrium between CO_2 and the carbonate followed by a rate-limiting electron transfer. The Tafel slopes provided by both Hackerman and Kanan are consistent with this mechanism with either a one- or two-electron transfer step, respectively. However, the proposal that CO_2 is initially reduced to $CO_2^{\bullet-}$ is not consistent with the data presented here.

Scheme 1. Proposed Mechanism for the Reduction of CO_2 to Formate on Sn/SnO_x Cathodes[a]

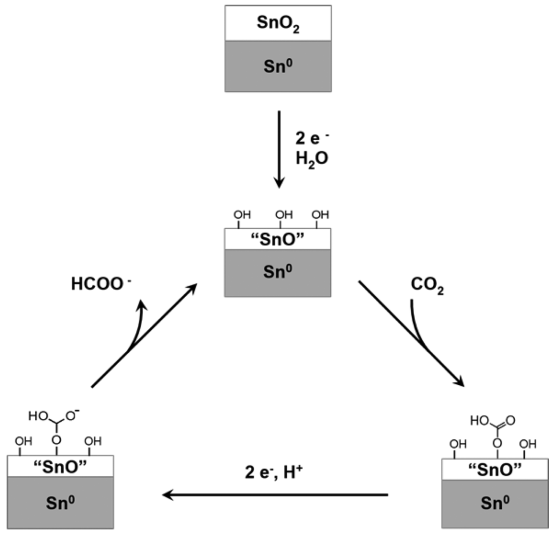

[a] Here "SnO" denotes a Sn^{II} oxyhydroxide species.

4. CONCLUSIONS

In conclusion, the electrochemical implications of the native tin oxide layer on the electrochemical reduction of CO_2 have been studied. In situ ATR-IR experiments demonstrate that, even under reducing potentials, a metastable oxide layer is present on tin cathodes. Analysis of the potential and time-dependent IR data indicates the formation and subsequent reduction of a surface-bound tin carbonate intermediate. Cyclic voltammetric analysis shows a redox couple at −1.0 V that corresponds to the SnO_2/SnO redox event. It was observed that this redox event is suppressed in a CO_2-saturated aqueous solution, as has recently been shown on indium cathodes.[8] The lack of reoxidation at slow scan rates is explained by the kinetically competing chemical process of carbonate formation on the Sn^{II} oxyhydroxide surface. This tin carbonate is not expected to be oxidizable in the potential regime studied. Potentiostatic bulk electrolysis experiments on $Sn_6O_4(OH)_4$ and SnO_2 nanoparticles show very little difference in the product distributions over a variety of potentials, which, coupled with voltammetric analysis, suggests that the catalytic species is the Sn^{II} oxyhydroxide surface.

These experiments rule out a single one-electron charge transfer to CO_2 to form $CO_2^{\bullet-}$ and instead pinpoint a surface-confined tin carbonate as the key electroactive intermediate. It is interesting that both indium and tin are formate-producing p-block metals that share the same oxide dependence on their CO_2 electrochemistry, specifically proceeding through a surface-bound carbonate. It is possible that similar chemistry may be observed on the entirety of the formate-producing p-block.

AUTHOR INFORMATION

Corresponding Author

*E-mail for A.B.B.: bocarsly@princeton.edu.

Author Contributions

[†]These authors contributed equally.

Notes

The authors declare no competing financial interest.

ACKNOWLEDGMENTS

The authors acknowledge the NSF (Grant CHE-1308652) for financial support. We also acknowledge Dr. Zachary Detweiler for fruitful discussions and assistance with the ATR-IR experiments. We thank Conor Thomas, Matthew Vallon, and Colleen Richardson for assistance with obtaining and interpreting XPS data. In addition, we acknowledge Marisa Sanders and Professor Robert Cava for help collecting XRD patterns. Finally, we thank Dr. István Pelczer, Kenith Conover, and John Schreiber for their assistance with NMR, thin film deposition, TEM, and SEM.

ABBREVIATIONS

ATR-IR, attenuated total reflectance infrared; IPCC, Intergovernmental Panel on Climate Change; PTFE, polytetrafluoroethylene; XPS, X-ray photoelectron spectroscopy; SEM, scanning electron microscopy; EDX, energy-dispersive X-ray spectroscopy; XRD, X-ray powder diffraction; TEM, transmission electron microscopy

REFERENCES

(1) Hartmann, D. L.; Klein Tank, A. M. G.; Rusticucci, M.; Alexander, L.; Broennimann, S.; Abdul-Rahman Charabi, Y.; Dentener, F.; Thorne, P.; Wild, M.; Zhai, P. In *Climate Change 2013: The Physical Science Basis. Contribution of Working Group I to the IPCC Fifth Assessment Report*; Stocker, T. F., Qin, D., Plattner, G.-K., Tignor, M., Allen, S. K., Boschung, J., Nauels, A., Xia, Y., Bex, V., Midgley, P. M., Eds.; Cambridge University Press: New York, 2014.

(2) Kunreither, H.; Gupta, S.; Bosetti, V.; Cooke, R.; Dutt, V.; Ha-Duong, M.; Held, H.; Llanes-Regueiro, J.; Patt, A.; Shittu, E.; Weber, E. In *Climate Change 2014: Mitigation of Climate Change. Contribution*

of Working Group III to the IPCC Fifth Assessment Report; Edenhofer, O., Pichs-Madruga, R., Sokona, Y., Farahani, E., Kadner, S., Seyboth, K., Adler, A., Baum, I., Brunner, S., Eickemeier, P., Kriemann, B., Savolainen, J., Schlömer, S., von Stechow, C., Zwickel, T., Minx, J. C., Eds.; Cambridge University Press: New York, 2014.

(3) Hori, Y. In *Modern Aspects of Electrochemistry*; Gamboa-Aldeco, M., Ed.; Springer: Berlin, 2008; pp 89−189.

(4) Bumroongsakulsawat, P.; Kelsall, G. H. *Electrochim. Acta* **2014**, *141*, 216−225.

(5) Anawati; Frankel, G. S.; Agarwal, A.; Sridhar, N. *Electrochim. Acta* **2014**, *133*, 188−196.

(6) Chen, Y.; Kanan, M. W. *J. Am. Chem. Soc.* **2012**, *134*, 1986−1989.

(7) Chen, Y.; Li, C. W.; Kanan, M. W. *J. Am. Chem. Soc.* **2012**, *134*, 19969−19972.

(8) Detweiler, Z. M.; White, J. L.; Bernasek, S. L.; Bocarsly, A. B. *Langmuir* **2014**, *30*, 7593−7600.

(9) Hsu, Y.-S.; Ghandhi, S. K. *J. Electrochem. Soc.* **1980**, *127*, 1592−1595.

(10) Gavrishchuk, E. M.; Vilkova, E. Y.; Timofeev, O. V.; Borovskikh, U. P.; Tikhonova, E. L. *Inorg. Mater.* **2007**, *43*, 579−583.

(11) Chandradass, J.; Bae, D. S.; Kim, K. H. *Adv. Powder Technol.* **2011**, *22*, 370−374.

(12) Jie, L.; Chao, X. *J. Non-Cryst. Solids* **1990**, *119*, 37−40.

(13) Choi, W.-K.; Jung, H.-J.; Koh, S.-K. *J. Vac. Sci. Technol., A* **1996**, *14*, 359−366.

(14) Tselesh, A. S. *Thin Solid Films* **2008**, *516*, 6253−6260.

(15) Langer, D. W.; Vesely, C. J. *Phys. Rev. B* **1970**, *2*, 4885−4892.

(16) Pourbaix, M. *Atlas of Electrochemical Equilibria*; Burgers, W. G., Ed.; Pergamon Press: London, 1974.

(17) Díaz, R.; Díez-Pérez, I.; Gorostiza, P.; Sanz, F.; Morante, J. R. *J. Braz. Chem. Soc.* **2003**, *14*, 523−529.

(18) Thornton, E. W.; Harrison, P. G. *J. Chem. Soc., Faraday Trans. 1* **1975**, *71*, 461−472.

(19) Thornton, E. W.; Harrison, P. G. *J. Chem. Soc., Faraday Trans. 1* **1975**, *71*, 2468−2477.

(20) Goel, R. G.; Prasad, H. S.; Bancroft, G. M.; Sham, T. K. *Can. J. Chem.* **1976**, *54*, 711−717.

(21) Smith, P. J.; Hill, R.; Nicolaides, A.; Donaldson, J. D. *J. Organomet. Chem.* **1983**, *252*, 149−152.

(22) McQuillan, A. J.; Hendra, P. J.; Fleischmann, M. *J. Electroanal. Chem.* **1975**, *65*, 933−944.

(23) Ortiz, R.; Márquez, O. P.; Márquez, J.; Gutiérrez, C. *J. Electroanal. Chem.* **1995**, *390*, 99−107.

(24) Abrahams, I.; Grimes, S. M.; Johnston, S. R.; Knowles, J. C. *Acta Crystallogr., Sect. C: Cryst. Struct. Commun.* **1996**, *52*, 286−288.

(25) Baur, W. H.; Khan, A. A. *Acta Crystallogr., Sect. B: Struct. Crystallogr. Cryst. Chem.* **1971**, *27*, 2133−2139.

(26) Hori, Y.; Wakebe, H.; Tsukamoto, T.; Koga, O. *Electrochim. Acta* **1994**, *39*, 1833−1839.

(27) Köleli, F.; Atilan, T.; Palamut, N.; Gizir, A. M.; Aydin, R.; Hamann, C. H. *J. Appl. Electrochem.* **2003**, *33*, 447−450.

(28) Kim, H.-Y.; Choi, I.; Ahn, S. H.; Hwang, S. J.; Yoo, S. J.; Han, J.; Kim, J.; Park, H.; Jang, J. H.; Kim, S.-K. *Int. J. Hydrogen Energy* **2014**, *39*, 16506−16512.

(29) Mizuno, T.; Ohta, K.; Sasaki, A.; Akai, T.; Hirano, M.; Kawabe, A. *Energy Sources* **1995**, *17*, 503−508.

(30) Kapusta, S.; Hackerman, N. *J. Electrochem. Soc.* **1983**, *130*, 607−613.

(31) Surdhar, P. S.; Mezyk, S. P.; Armstrong, D. A. *J. Phys. Chem.* **1989**, *93*, 3360−3363.

(32) Lamy, E.; Nadjo, L.; Savéant, J. M. *J. Electroanal. Chem. Interfacial Electrochem.* **1977**, *78*, 403−407.

(33) Schwarz, H. A.; Dodson, R. W. *J. Phys. Chem.* **1989**, *93*, 409−414.

(34) Koppenol, W. H.; Rush, J. D. *J. Phys. Chem.* **1987**, *91*, 4429−4430.

(35) Fletcher, S. *J. Solid State Electrochem.* **2009**, *13*, 537−549.

(36) Yamamoto, M.; Yoshida, T.; Yamamoto, N.; Yoshida, H.; Yagi, S. *e-J. Surf. Sci. Nanotechnol.* **2014**, *12*, 299−303.